Diabatic Surfaces and the Pathway for Primary Electron Transfer in a Photosynthetic Reaction Center

Massimo Marchi,[†,‡] John N. Gehlen,[†] David Chandler,*[,†] and Marshall Newton[§]

Contribution from the Department of Chemistry, University of California, Berkeley, California 94720, Department of Chemistry, Brookhaven National Laboratory, Upton, New York 11973, and CECAM Université Paris-Sud, 91405 Orsay, France

Received October 8, 1992

Abstract: We have performed molecular dynamics simulations for two different models of a photosynthetic reaction center (*Rps. viridis*) to examine the diabatic surfaces governing the primary charge separation after photoexcitation. We include the electrostatic energy of the entire proteic complex and also account for the energies of the electronic states of chromophores as computed by semiempirical quantum theory. The statistics we have acquired from our dynamics trajectories is sufficient to contrast the behaviors of the two models, to deduce the effects of crystallization water, and to measure the size of nonlinear response on the pertinent diabatic surfaces. Further, with the perspective we develop, we are able to juxtapose the active and inactive branches of the reaction center. By renormalizing our computed diabatic surfaces with a physically reasonable value for the high-frequency dielectric response of the system, the simulation results can be brought into accord with experimental observations of the thermodynamic driving force for the primary electron transfer. With no further adjustment, we find that the diabatic surfaces for the excited special pair state, SP*, and the charge-separated state SP^+–BPL^- intersect with essentially no activation barrier. Here, BPL refers to the bacteriopheophytin on the L branch. In contrast, the SP* and SP^+–BPM^- surfaces intersect in the normal region with an activation barrier and an endothermic thermodynamic driving force. A related observation is that we find fluctuations in the pertinent energy gaps to be significantly smaller on the active L branch than they are on the inactive M branch. We also examine the surfaces associated with moving charge to the accessory bacteriochlorophylls, BCL and BCM. We find that these surfaces lie at energies far above SP*. This finding excludes the possibility of a two-step mechanism within our model for the primary charge transfer; it agrees roughly with Thompson and Zerner's estimate based on a dielectric continuum model. We make simple estimates based upon a superexchange mechanism with physically reasonable nearest-neighbor electronic coupling that indicate our computed diabatic surfaces are consistent with the experimentally observed kinetics of the primary electron transfer. We consider also the temperature dependence of the forward rate and the ratio of the rate of the back-reaction, SP^+–$BPL^- \rightarrow$ SP to the rate of the forward reaction. Here, we carry out quantal analyses based upon our computed spectral densities for the energy gap fluctuations.

1. Introduction

This paper describes the molecular dynamics simulation, results, and interpretation of primary electron transfer in the bacterial photosynthetic reaction center, *Rhodopseudomonas* (*Rps.*) *viridis*.

Interest in the chemical physics of photosynthetic reaction centers (RC) has been spurred by X-ray crystallographic elucidation of the structures of two such systems.[1,2] In the purple bacteria *Rps. viridis*, the RC is composed of chromophores (pigments) and four proteic subunits (C, L, M, and H) which provide the necessary scaffolding to hold the chromophores in place. The pigment molecules include four bacteriochlorophyll *b* (BC), two bacteriopheophytin *b* (BP), and two quinone molecules. The RC has two proteic branches (L and M) which exhibit an approximate 2-fold rotation symmetry. The two branches are joined by a bacteriochlorophyll *b* dimer, the so-called special pair (SP). See Figure 1.

The primary charge separation is the focus of much of the current research, both experimentally and theoretically.[3-12] This process is the transfer of an electron from the photoexcited special pair, SP*, to BPL. The primary charge separation has many puzzling features. Despite a large center-to-center distance of ~17 Å between SP and BPL, the electron transfer is very fast, occurring in roughly 10 ps or less. Further, even with the near-C_2 symmetry of the RC, the reaction occurs only along the L branch. Additionally, there is debate about the role of the accessory bacteriochlorophyll (BCL) in the electron transfer. These features are the primary concern of the molecular modeling and computer simulations presented herein.

We consider, in particular, the energetics of nuclear reorganization. We examine the different electronic diabatic surfaces by computing probability distributions and autocorrelation functions for the energy gaps between the surfaces. We also simulate nonequilibrium relaxation to determine the consequences of nonlinear effects. A similar approach has proved useful in analyzing the mechanism of aqueous ferrous–ferric electron

† University of California.
‡ Université Paris-Sud.
§ Brookhaven National Laboratory.

(1) Deisenhofer, J.; Epp, O.; Miki, K.; Huber, R.; Michel, H. *J. Mol. Biol.* **1984**, *180*, 385.
(2) Chang, C. H.; Tiede, D.; Tang, J.; Smith, U.; Norris, J.; Schiffer, M. *FEBS Lett.* **1986**, *205*, 82.
(3) Vos, M. H.; Lambry, J. C.; Robles, S. J.; Youvan, D. C.; Breton, J.; Martin, J.-L. *Proc. Natl. Acad. Sci. U.S.A.* **1991**, *88*, 8885.
(4) Du, M.; Rosenthal, S. J.; Xie, X.; DiMagno, T. J.; Schmidt, M.; Hanson, D. K.; Schiffer, M.; Norris, J. R.; Fleming, G. R. *Proc. Natl. Acad. Sci. U.S.A.* **1992**, *89*, 8517–8521.
(5) Moser, C. C.; Keske, J. M.; Warncke, K.; Farid, R. S.; Dutton, P. L. *Nature* **1992**, *355*, 796.
(6) Lockhart, D. J.; Goldstein, R. F.; Boxer, S. G.; *J. Chem. Phys.* **1988**, *89*, 1408. Boxer, S. G.; Goldstein, R. A.; Lockhart, D. J.; Middendorf, T. R.; Takiff, L. *J. Phys. Chem.* **1989**, *93*, 8280–8294.
(7) Martin, J. L.; Breton, J.; Hoff, A. J.; Migus, A.; Antonetti, A. *Proc. Natl. Acad. Sci. U.S.A.* **1986**, *83*, 957. Breton, J.; Martin, J.-L.; Migus, A.; Antonetti, A.; Orszag, A. *Proc. Natl. Acad. Sci. U.S.A.* **1986**, *83*, 5121.
(8) Holzapfel, W.; Finkele, U.; Kaiser, W.; Oesterhelt, D.; Scheer, H.; Stilz, H. U.; Zinth, W. *Chem. Phys. Lett.* **1989**, *160*, 1.
(9) Marcus, R. A. *Chem. Phys. Lett.* **1987**, *133*, 471. Marcus, R. A. *Chem. Phys. Lett.* **1988**, *146*, 13. Marcus, R. A. In *Current Research in Photosynthesis*; Baltscheffsky, Ed.; Kluwer Academic Publishers: The Netherlands, 1990; Vol. 1, p 1.
(10) Michel-Beyerle, M. E.; Plato, M.; Deisenhofer, J.; Michel, H.; Bixon, M.; Jortner, J. *Biochim. Biophys. Acta* **1988**, *932*, 52.
(11) Friesner, R. A.; Won, Y. *Biochim. Biophys. Acta* **1989**, *977*, 99.

0002-7863/93/1515-4178$04.00/0

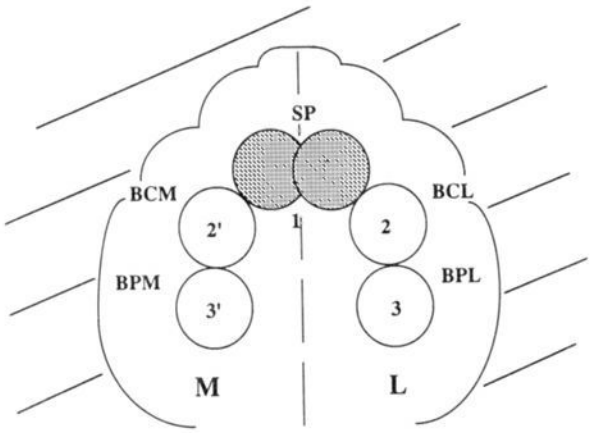

Figure 1. Schematic view of the reaction center showing the special pair (SP) of bacteriochlorophylls, the accessory bacteriochlorophylls (BCM and BCL) of the M and L branches, and the bacteriopheophytins (BPM and BPL). The surrounding proteic environment is depicted by the widely spaced hatched lines. The vertical dashed line denotes the line of near-C_2 rotational symmetry. In its photoexcited state, an electronic charge is distributed over the special pair. We refer to this state as SP* or state 1. Soon after excitation, an electron is transferred to BPL forming SP^+–BPL^-, which we refer to as state 3. In this paper, we study the energetics of the proteic complex for each of the five states, 1, 2′(SP^+–BCM^-), 2(SP^+–BCL^-), 3′(SP^+–BPM^-), and 3. The energetics as a function of nuclear configurations allows us to predict the pathway of the primary electron transfer, $1 \rightarrow 3$, and to understand the inactivity of the M branch, i.e., $1 \not\rightarrow 3'$.

transfer.[13] The RC protein system, of course, has a far more complicated atomic structure than liquid water. Further, the RC possesses more than two pertinent redox states. This latter feature, as we shall see, leads to a phenomenology somewhat more general than that usually conceived of in the simplest Marcus pictures of electron transfer.[14,15]

We are not the first to use molecular modeling and molecular dynamics to investigate the energetics of nuclear reorganizations pertinent to electron transfer in the RC.[16,17] We feel that our calculations represent a significant improvement over this earlier work, and the conclusions we draw are new. A detailed comparison is made in Section 6. The results we report herein are arrived at from many long trajectories. Our results appear to be reproducible with relatively small statistical uncertainties. The statistical quality is sufficient to discern significant differences between the diabatic surfaces on the active and inactive branches of the RC. Further, we can summarize many of our results in terms of a reduced model of three states coupled to a dissipative linear bath—a generalization of the often-studied spin-boson model.[18,19]

In the presentation that follows, we begin in Section 2 with the description of this reduced model. This phenomenology provides guidance as to which quantities should be studied in the molecular dynamics simulation. Section 3 deals with the description of the potential fields and simulation parameters used in our molecular dynamics calculations. Section 4 gives a description of our simulation results. In Section 5, these results are scaled using the experimentally observed thermodynamic driving force[20,21] of the primary electron transfer and the semiempirical electronic structure energies of Thompson and Zerner.[22] We conclude in Section 7 with a discussion of the dynamical mechanism of the primary electron transfer and comparisons of theory and experiment. An Appendix discusses the role of electronic polarization. The formulas derived there pertain to the scaling carried out in Section 5.

2. Reduced Model for Electron Transfer

The electron transfer between a donor and an acceptor immersed in a dielectric medium can be modeled very simply by a two-level system coupled to the fluctuating field of a bath.[18,19] This is the physical model underlying the Marcus theory for electron transfer.[14,15] In the nonadiabatic or weak coupling limit, the resonance state between donor and acceptor is reached by means of thermal fluctuations of the bath. Only at or near resonance, the electron can tunnel between the reactant and product sites.

A similar picture can be used for a system like the RC where an additional intermediate state (the charged accessory bacteriochlorophyll) is present (see Figure 1). Consider the electron transfer along one of the two possible routes (L or M). The three redox states coincide with (1) the state where the special pair is photoexcited but neutral, SP* (for simplicity we make no distinction between the singlet and triplet forms); (2) the state where the transferring electron resides on the accessory bacteriochlorophyll of the L branch, BCL (i.e., the redox state is SP^+–BCL^-); and (3) the state where the electron resides on the bacteriopheophytin of the L branch, BPL (i.e., the redox state is SP^+–BPL^-). For transfer on the M branch, we have states 2′ and 3′ corresponding to SP^+–BCM^- and SP^+–BPM^-, respectively.

For electron transfer occurring along the L branch, we imagine the Hamiltonian

$$H = \sum_{\alpha=1}^{3} |\alpha\rangle H_\alpha \langle\alpha| + [|1\rangle H_{12}\langle 2| + |2\rangle H_{21}\langle 1|] + [|2\rangle H_{23}\langle 3| + |3\rangle H_{32}\langle 2|] \quad (2.1)$$

Here, H_α is the diabatic Hamiltonian for the nuclei when the system is in the redox state α. For simplicity, we assume that the interstate couplings are independent of the accessible nuclear coordinates. Further, since the special pair is at a relatively large distance from the pheophytin, we neglect the direct coupling between states 1 and 3.

For electron transfer on the inactive M branch, the schematic Hamiltonian is essentially the same as that in eq 2.1. The difference is that state 2 is replaced by state 2′, and state 3 is replaced by state 3′.

The energy gap between states 1 and 3,

$$\Delta E_{13} = H_3 - H_1 \quad (2.2)$$

is a function of the nuclear coordinates which at any time t can be written as

$$\Delta E_{13}(t) = -\mathcal{E}_\parallel(t) + \Delta\epsilon_3 \quad (2.3)$$

Here,

(12) Wraight, C. A.; Clayton, R. K. *Biochim. Biophys. Acta* **1974**, *333*, 246.
(13) Bader, J. S.; Chandler, D. *Chem. Phys. Lett.* **1989**, *157*, 501.
(14) Marcus, R. A. *J. Chem. Phys.* **1956**, *24*, 966. Marcus, R. A. *J. Chem. Phys.* **1956**, *24*, 979.
(15) Marcus, R. A.; Sutin, N. *Biochim. Biophys. Acta* **1985**, *811*, 265. Newton, M. D.; Sutin, N. *Annu. Rev. Phys. Chem.* **1984**, *35*, 437.
(16) (a) Creighton, S.; Hwang, J.-K.; Warshel, A.; Parson, W. W.; Norris, J. *Biochemistry* **1988**, *27*, 774. (b) Warshel, A.; Chu, Z.-T.; Parson, W. W. *Science* **1989**, *246*, 112. (c) Parson, W. W.; Nagarajan, V.; Gaul, D.; Schenck, C. C.; Chu, Z.-T.; Warshel, A. In *Reaction Centers of Photosynthetic Bacteria*; Michel-Beyerle, M. E., Ed.; Springer: Berlin, 1990; p 239. (d) Parson, W. W.; Chu, Z.-T.; Warshel, A. *Biochim. Biophys. Acta* **1990**, *1017*, 251.
(17) (a) Treutlein, H.; Schulten, K.; Deisenhofer, J.; Michel, H.; Brunger, A.; Karplus, M. In *The Photosynthetic Bacterial Reaction Center: Structure and Dynamics*; Breton, J., Vermeglio, A., Eds.; Plenum Press: London, 1988; p 139. (b) Treutlein, H.; Schulten, K.; Niedermeier, J.; Deisenhofer, J.; Michel, H.; DeVault, D. In *The Photosynthetic Bacterial Reaction Center: Structure and Dynamics*; Breton, J., Vermeglio, A., Eds.; Plenum Press: London, 1988; p 369. (c) Treutlein, H.; Schulten, K.; Brunger, A. T.; Karplus, M.; Deisenhofer, J.; Michel, H. *Proc. Natl. Acad. Sci. U.S.A.* **1992**, *89*, 75–79. (d) Schulten, K.; Tesch, M. *Chem. Phys.* **1991**, *158*, 421.
(18) Leggett, A. J.; Chakravarty, S.; Dorsey, A. T.; Fisher, M. P. A.; Garg, A.; Zwerger, W. *Rev. Mod. Phys.* **1987**, *59*, 1.
(19) Chandler, D. In *Les Houches. Part 1. Liquids, Freezing and the Glass Transition*; Levesque, D., Hansen, J. P., Zinn-Justin, J., Eds.; Elsevier, B. V.: North Holland, 1991; pp 193–285.
(20) Goldstein, R. A.; Takiff, L.; Boxer, S. G. *Biochim. Biophys. Acta* **1988**, *934*, 253.
(21) Ogrodnik, A.; Volk, M.; Letterer, R.; Feick, R.; Michel-Beyerle, M. E. *Biochim. Biophys. Acta* **1988**, *936*, 361.
(22) Thompson, M. A.; Zerner, M. C. *J. Am. Chem. Soc.* **1991**, *113*, 8210.

$$\Delta\epsilon_3 = \langle \Delta E_{13} \rangle_1 \tag{2.4}$$

where $\langle ... \rangle_1$ indicates the equilibrium ensemble average with Hamiltonian H_1. The dynamical variable $-\mathcal{E}_\parallel(t)$ is the instantaneous fluctuation of that energy gap from its average. We use the subscript notation $\parallel$ since the variable is akin to a local nuclear polarization field that is parallel to an axis connecting SP and BPL.

Similarly, we can always partition the 1–2 energy gap into its average, a contribution from $\mathcal{E}_\parallel(t)$, and an additional variable, $\mathcal{E}_\perp(t)$. That is,

$$\Delta E_{12} = -\mathcal{E}_\perp(t) - b\mathcal{E}_\parallel(t) + \Delta\epsilon_2 \tag{2.5}$$

with

$$\Delta\epsilon_2 = \langle \Delta E_{12} \rangle_1 \tag{2.6}$$

and for conceptual reasons (see below) the constant b is chosen so that, at equal times, $\mathcal{E}_\parallel$ and $\mathcal{E}_\perp$ are statistically orthogonal,

$$\langle \mathcal{E}_\parallel \mathcal{E}_\perp \rangle_1 = 0 \tag{2.7}$$

From this perspective of the system, the dynamics of the primary electron transfer is governed in large part by the dynamics of $\mathcal{E}_\perp(t)$ and $\mathcal{E}_\parallel(t)$. In subsequent sections of this paper, we show that these dynamical variables obey linear response to a reasonable approximation. This behavior is suggestive of the effective diabatic Hamiltonians,

$$\begin{aligned} H_1 &\approx H_B \\ H_2 &\approx H_B - b\mathcal{E}_\parallel - \mathcal{E}_\perp + \Delta\epsilon_2 \\ H_3 &\approx H_B - \mathcal{E}_\parallel + \Delta\epsilon_3 \end{aligned} \tag{2.8}$$

where H_B is a harmonic bath Hamiltonian, and $\mathcal{E}_\parallel$ and $\mathcal{E}_\perp$ are linear functions of the normal modes of that bath. Such a system is a three-state generalization of the standard spin-boson model.[18,19] The corresponding model for the M branch is developed similarly with, for example, $\mathcal{E}_\parallel$ and $\mathcal{E}_\perp$ replaced by the variables $\mathcal{E}'_\parallel$ and $\mathcal{E}'_\perp$. To the extent that the linear approximation is adequate, $\mathcal{E}_\perp(t)$ and $\mathcal{E}_\parallel(t)$ are Gaussian variables, and their classical dynamics are completely characterized by the correlation functions

$$\begin{aligned} C_\parallel(t) = \langle \mathcal{E}_\parallel \mathcal{E}_\parallel(t) \rangle_1 \qquad C_\perp(t) = \langle \mathcal{E}_\perp \mathcal{E}_\perp(t) \rangle_1 \\ C_{cross}(t) = \langle \mathcal{E}_\perp \mathcal{E}_\parallel(t) \rangle_1 \end{aligned} \tag{2.9}$$

Note that in general $C_{cross}(t) \neq 0$ for $t \neq 0$, since the orthogonality of the two variables cannot persist exactly to finite times in a dissipative system. Nevertheless, we will see that $C_{cross}(t)$ is extremely small.

The probability distribution functions for the energy gaps are

$$\begin{aligned} P_{12}(x) &= \langle \delta(x - \Delta E_{12}) \rangle_1 \\ P_{13}(x) &= \langle \delta(x - \Delta E_{13}) \rangle_1 \end{aligned} \tag{2.10}$$

To the extent that $\mathcal{E}_\parallel$ and $\mathcal{E}_\perp$ are Gaussian random variables, both $P_{12}(x)$ and $P_{13}(x)$ will be Gaussian distributions, and the free energy governing $\mathcal{E}_\parallel$ and $\mathcal{E}_\perp$ will be parabolic for any of the three diabatic states. Specifically, the free energies will be

$$\begin{aligned} F_1 &= F_B \\ F_2 &= F_B - b\mathcal{E}_\parallel - \mathcal{E}_\perp + \Delta\epsilon_2 \\ F_3 &= F_B - \mathcal{E}_\parallel + \Delta\epsilon_3 \end{aligned} \tag{2.11}$$

where

$$F_B = \frac{1}{2\alpha_\parallel}\mathcal{E}_\parallel^2 + \frac{1}{2\alpha_\perp}\mathcal{E}_\perp^2 \tag{2.12}$$

with

$$\alpha_\parallel = \beta\langle (\delta\mathcal{E}_\parallel)^2 \rangle_1 \qquad \alpha_\perp = \beta\langle (\delta\mathcal{E}_\perp)^2 \rangle_1 \tag{2.13}$$

and $\beta^{-1} = k_B T$. Note that the average values of $\mathcal{E}_\parallel(t)$ and $\mathcal{E}_\perp(t)$ in state 1 are zero due to our definition of H_1.

An important consequence of the Gaussian or linear approximation is the ability to quantize the system on the basis of what is learned from the classical molecular dynamics.[19] In particular, the spectral densities for the energy gap fluctuations are obtained directly from the Fourier transforms, such as

$$\tilde{C}_\parallel(\omega) = \int_{-\infty}^{\infty} dt\, C_\parallel(t) \cos \omega t \tag{2.14}$$

In the regime of weak interstate coupling, well-known expressions relate the spectral densities to rate constants for electron transfer.[23] Outside this regime, or for time scales where rate constants are not well defined, a more general numerical analysis of the quantum dynamics is necessary.[24] In any case, the knowledge of the spectral densities provides the starting point for the calculations.

We now turn to the detailed atomistic models for the RC from which we will compute the quantities described in this section.

3. Atomistic Model and Simulation Technique

We have constructed two atomistic models, I and II. For both, the calculations we have performed were based on the X-ray structure of the reaction center of *Rps. viridis* at 2.3-Å resolution[25] taken from the Brookhaven protein data bank. The terminal groups of subunits L, M, C, and H were formed by replacing the amide or carbonyl group respectively with a positively charged N-terminus and a negatively charged C-terminus. For each of the subunits we chose as the terminus the last amino acid of the series with known X-ray position. The coordinates of the ubiquinone chain (not known experimentally) were generated by computer graphics in order to minimize the hindrance with the neighboring groups.

For the protein subunits we used the potential parameters and the topology definition of the CHARMm data base.[26] We did not include the stretching term of the potential-energy function. The bonds were kept rigid by the SHAKE constraint algorithm.[27] Nonpolar hydrogens were not explicitly included in the model. The Verlet leap frog integrator[28] (with a time step of 0.8 fs) was used to numerically solve the Newtonian equations of motion. For the purposes of performing the dynamics (but not for computing electrostatic contributions to energy gaps; see below), a spherical cutoff of 10 Å was applied to the nonbonded interactions. The discontinuity in the potential function cutoff was smoothed out to zero by a third-order spline between 9 and 10 Å. All the simulation runs of our study were carried out with the molecular dynamics program ORAC developed by one of us (M.M.).

Concerning the chromophores, in model I, the CHARMm potential parameters for bacteriochlorophyll *a* were utilized for bacteriochlorophylls *b* by unsaturating the single CC bond attached to the third pyrrole ring. We redefined the type of the atoms involved consistently with the CHARMm types and redistributed the charge by placing –0.1e on the carbon and +0.1e

(23) Calculations of this type have been done for an inorganic exchange by: Bader, J. S.; Kuharski, R. A.; Chandler, D. *J. Chem. Phys.* **1990**, *93*, 230; for a proteic reaction by: Zheng, C.; McCammon, J. A.; Wolynes, P. G. *Chem. Phys.* **1991**, *158*, 261. Warshel's so-called "dispersed polaron" model (e.g., ref 16b) is similar though published implementations include a semiclassical approximation which incurs large errors whenever quantum effects are significant (see discussion by Bader et al.).

(24) Mak, C. H.; Chandler, D. *Phys. Rev. A* **1990**, *41*, 5709; **1991**, *44*, 2352. Mak, C. H. *Phys. Rev. Lett.* **1992**, *68*, 899. Mak, C. H.; Gehlen, J. N. *Chem. Phys. Lett.*, in press.

(25) Deisenhofer, J.; Michel, H. *Science* **1989**, *245*, 1463.

(26) Brooks, B. R.; Bruccoleri, R. E.; Olafson, B. D.; States, D. J.; Swaminathan, S.; Karplus, M. *J. Comput. Chem.* **1983**, *4*, 187. The potential parameters and topology used in the simulation were taken from Polygen Corp. Parameter and Topology files for CHARMm, Version 20, copyright 1986, released Aug 1988.

(27) Ryckaert, J. P.; Ciccotti, G.; Berendsen, H. J. C. *J. Comput. Phys.* **1977**, *23*, 327.

(28) Hockney, R. W. *Methods Comput. Phys.* **1970**, *9*, 136.

on the hydrogen. For the remaining chromophores we assigned the atomic types according to the CHARMm categories and used an united atom approach for the nonpolar hydrogens. Since the menaquinone-7 (MQ7) and ubiquinone-1 (UQ1) are far away from the regions involved in the primary charge separation, their electrostatic potential was modeled in a simple way. We assigned charges –0.55e and 0.55e respectively to the oxygen and carbon of the carbonyl groups. The charges of the ester groups of UQ1 were chosen to be 0.1, –0.3, and 0.2e respectively for the sp^2 ring carbon, the oxygen, and the methyl group. All the charges on the remaining atoms and on all the atoms of the dihydroneurosporene (NS1) were set to zero.

For the model II chromophores, we used the parameterization of the prosthetic groups made by Treutlein et al.[17a,b] and available recently with the XPLOR program.[29] Model II also included the crystallization water molecules and the detergent molecule dimethylaminolauryl oxide. The latter molecule was parameterized according to Treutlein et al.[17a,b] The simple point charge (SPC) model was used for water. Neither the crystallization water nor the detergent was included in model I. The charge states for the amino acids were those for pH = 7, assuming standard p*K* values, except for glutamate L104 that was protonated in model II, but nonprotonated in model I. A dielectric constant of 1 was used for both models. The number of crystallographically resolved water molecules is 201, nearly all of which are in the interior of the proteic complex.

The RC is a membrane protein, embedded in the phospholipid bilayers and surrounded on the sides of the subunits H and C by a water solution of respectively cytoplasm and peryplasm. A realistic simulation of an accurate model of the full system is for the moment computationally prohibitive. However, various experiments in the past have shown that the primary electron transfer is only mildly sensitive to changes in temperature.[30] As a result, it is plausible that the bilayer and exterior water solvation have only a small effect on the primary electron transfer. We have thus chosen to simulate a system which included only the RC and have ignored the effects due to the external environment. Moreover, only a portion of the total number of atoms of the RC were treated dynamically; the rest were treated statically. We divided the system into two regions: a primary simulation region where the Newtonian equations of motion were solved explicitly and a secondary region where the atoms were kept fixed at their X-ray positions. The atoms of the primary region moved under the potential field produced by themselves and by the secondary atoms. The simulation was run in the microcanonical ensemble. With regard to the alternative boundary conditions used by other groups to simulate the RC (e.g., stochastic boundaries), our choice of simulation method has the advantage that there is always a conserved quantity (i.e., the total energy) that can be used as a quality control for our MD simulation.

We picked as the primary region an area of the RC which surrounds the central chromophores. In particular, six spheres of radius r_0 are each centered on the center of masses of the pyrrole rings of the SP, BC, and BP on the L and M sides. Atoms lying within the volume formed from the union of these spheres are the primary atoms. For model I and II we chose respectively r_0 = 20 Å and r_0 = 23 Å. This yielded a primary region of 4945 atoms for model I and of 5550 atoms for model II. There are 74 crystallization water molecules among those atoms in the primary region of model II. We carried out a few short trajectories with larger values of r_0 to convince ourselves that our computed averages and correlation functions were reasonably insensitive to increasing the size of the primary region.

The initial stage of the MD simulation for both models involved an equilibration period of 60 ps where the atomic velocities were scaled every 2 ps to thermalize the system around 300 K. A typical data acquisition run lasted 60 ps. Because of the large system size and length of the simulation, it would have been impractical to store all of the instantaneous atomic configurations for the length of the run. Thus, to gather time-dependent information relevant to the electron transfer, every 2.4 fs we have calculated and stored the local field on the four nitrogens of each pyrrole ring. We stress that our potential energy cutoffs affect the dynamics, but, when computing the energy gaps, contributions from all the atoms of the RC were included.

(29) Brunger, A. T. In *Crystallographic Computing 4: Techniques and New Technologies*; Isaacs, N. W.; Taylor, M. R., Eds.; Oxford, Clarendon Press, 1988. We acquired the XPLOR parameter and topology files through the data base available on the CRAY-YMP at the San Diego Super Computer Center.

(30) Fleming, G. R.; Martin, J. L.; Breton, J. *Nature* **1988**, *333*, 190.

4. Simulation Results

4.1. Structure of the Reaction Center. We have first compared the X-ray coordinates of the RC with the calculated averaged structures of our two models. This comparison provides a simple means to assess how close the calculated phase space minimum is to the experimental one. We found that both models reproduced the experimental structure with an overall root-mean-square (rms) displacement for the chromophores below 2 Å. We obtain 1.7 Å and 1.3 Å respectively for models I and II. In both cases the rms displacement from the X-ray positions was larger for the phytol and quinoid chains. This finding is in accord with the results of previous simulations of the RC.[17a,c]

As an indication of the atomic mobility, we have calculated the root-mean-square displacement from the average structure. The results for the two models are very similar. For model II, we have found an overall value of 0.2 Å per atom. This global number cannot be directly related to experimental observations since it includes contributions from atoms at the borders of the primary region, which are most affected by the boundary conditions. For the bacteriochlorophylls and bacteriopheophytins we have found a rms displacement of 0.3 Å which is in close agreement with the experimental value of 0.4 Å.[17c] The mobility of the phytol chains is larger than those of the pyrrole rings, with a rms displacement of 0.5 Å. An interesting feature that we observed with model II is the high mobility of a few crystallization waters. Although the average rms displacement for the 74 water molecules included in the calculation is 0.5 Å, the rms displacements of waters 46, 51, 93, 95, 155, and 159 are above 1.0 Å.

4.2. Fluctuations of the Energy Gap. If the exchanged electron interacts with the proteic environment only through an electrostatic pseudopotential, the electrostatic energy $V_\alpha(t)$ of the electron when at the chromophore α is the only relevant part of the diabatic Hamiltonians. Note that to calculate the potential of the electron due to the proteic environment, one must subtract an electronic charge from the special pair. In particular, let $\{q_i\}$ denote the set of all charges used in our molecular dynamics simulation of the SP* state. To compute V_α, we use the related set of charges,

$$\begin{aligned} z_i &= q_i + e/8, \text{ for site } i \text{ being a nitrogen} \\ &\qquad \text{atom in the special pair} \\ &= q_i, \text{ otherwise} \end{aligned} \tag{4.1}$$

where $-e$ is the charge of an electron. Then

$$V_\alpha = \frac{1}{n} \sum_{j \in \alpha} \sum_{i \notin \alpha} \frac{-e z_i}{r_{ij}} \tag{4.2}$$

where j is summed over all nitrogens sites in chromophore α (there are n = 8 such sites in the special pair, and n = 4 in the other four chromophores: BCL, BCM, BPL, and BPM), and the index i is summed over all partially or fully charged sites (nitrogen or otherwise) throughout the proteic system but *not* within chromophore α. Note that, in this formulation of V_α, we imagine that the charge distribution of the transferring electron is uniformly distributed on the nitrogens. (We have considered the energetic consequences of varying this distribution within a given chromophore and find them to be small. See Section 5.) During the simulations, we calculated $V_\alpha(t)$ on every chromophore of the functional (L) and nonfunctional (M) branches.

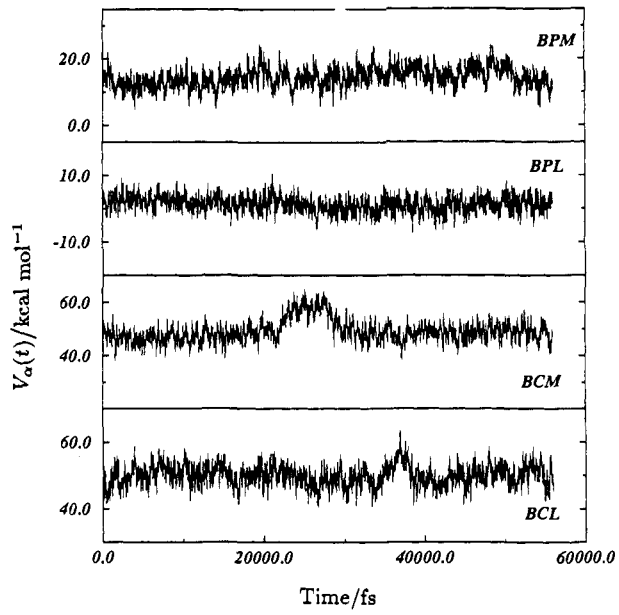

Figure 2. Electrostatic energies versus simulation time: results for model II. We plot $V_\alpha(t)$ (see text) for four chromophores.

The potential energy difference between two chromophores α and β, $V_\alpha - V_\beta$, is the energy gap or the vertical excitation energy for electron transfer from α to β. For example,

$$\Delta E_{12} = V_{BCL} - V_{SP}$$
$$\Delta E_{13} = V_{BPL} - V_{SP} \qquad (4.3)$$

and similarly for energy gaps on the M branch. These are the basic energy gaps studied in our simulation. Scaled and shifted energy gaps which incorporate information from quantum chemical calculations are considered in Section 5.

For model I, which did not include the waters, we found that for all chromophores $V_\alpha(t)$ fluctuated as if there was a monostable free energy surface. For model II instead, we found a more complex behavior. We show in Figure 2 a plot of the electrostatic energy versus simulation time for the bacteriopheophytins and accessory bacteriochlorophylls on the L and M sides. Visual inspection of Figure 2 indicates that the electric potential fluctuates significantly less at the BPL site than at the site of BPM or BCL or BCM. Further, while the energy fluctuations of BPL and BPM are uneventful, transitions from one configurational state to another and back can be observed for BCL and BCM. Such events occur only once within 56 ps of simulation. This transition is probably due to a polar group isomerization in the neighboring amino acid side chains of the bacteriochlorophylls.

We have computed the time correlation functions of the energy gap fluctuations, defined as

$$C_{ij}(t - t') = \langle \delta E_{ij}(t) \delta E_{ij}(t') \rangle_1 \qquad (4.4)$$

where $\delta E_{ij}(t) = \Delta E_{ij}(t) - \langle \Delta E_{ij} \rangle_1$. Here, i and j refer to the state labels 1, 2, 3, 2′, and 3′. The subscript 1 labeling the average indicates that the trajectory from which it is obtained is carried out with the potential energy we associate with state 1, SP*. Linear combinations of $C_{12}(t)$, $C_{13}(t)$, and $C_{23}(t)$ yield the correlation functions $C_\parallel(t)$, $C_\perp(t)$, and $C_{cross}(t)$ defined in Section 2. Figures 3 and 4 show the time dependence of $C_{1j}(t)$, j = 2, 3, 2′, and 3′, for models I and II. In the calculation of the time correlation function of model II involving BCL and BCM, we did not include the periods of time over which, due to isomerization, $V_{BCL}(t)$ and $V_{BCM}(t)$ differed markedly from their average. The fact that these isomerizations can occur spontaneously indicates some significant degree of nonlinearity in the proteic system's response. Furthermore, in view of these isomerizations, it would seem that any viable mechanism for electron transfer cannot require a very limited range of values for V_{BCL}. We will focus on these aspects shortly.

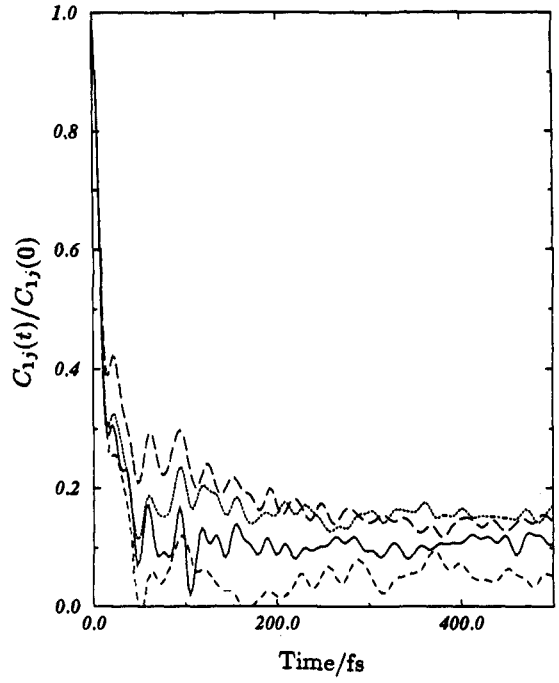

Figure 3. Time correlation functions of the energy gaps for model I. We show results for $C_{12}(t)/C_{12}(0)$ (continuous line), $C_{13}(t)/C_{13}(0)$ (short-dashed lines), $C_{12'}(t)/C_{12'}(0)$ (dashed line), and $C_{13'}(t)/C_{13'}(0)$ (long dashed line).

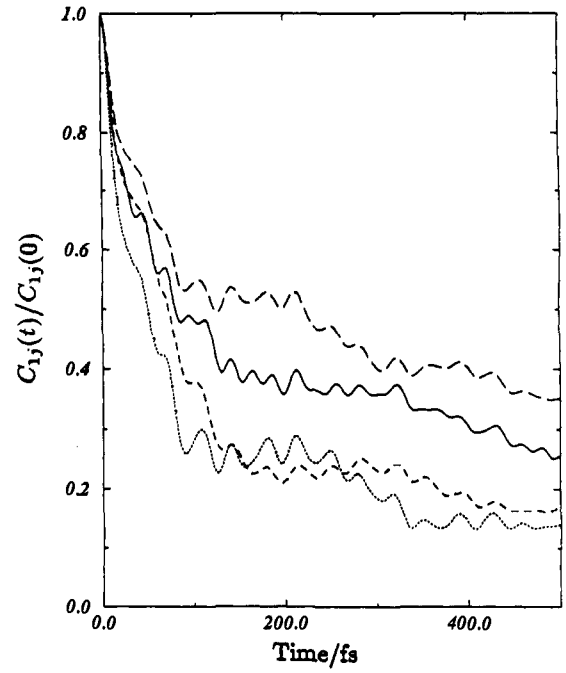

Figure 4. Time correlation functions of the energy gaps for model II (lines same as in Figure 3).

For both models we observe an initial fast decay of the correlation function followed by a slow relaxation regime. However, the relaxation lifetimes of the two regimes are different for the two models. The fast relaxation has a decay time of ~50 fs for model I, while it is ~100 fs for model II. In the same fashion, in the slow relaxation regime, the correlation functions calculated for model I decay more quickly than for model II. This slow decay of the time correlation functions is suggestive of glassy behavior in the RC. This behavior is more marked in the simulation with model II.

4.3. Shape of the Free Energy Surfaces. The straightforward mapping between the energy gaps and the fields coupled to the

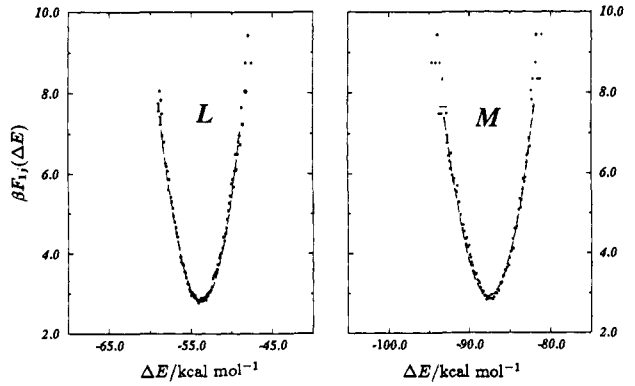

Figure 5. Energy gap free energy surfaces in units of k_BT for model I. The filled circles are the results from simulations and the dashed lines are a second-order polynomial fit. The left panel shows the free energy $F_{13}(\Delta E)$ and the right panel shows the free energy $F_{13'}(\Delta E)$.

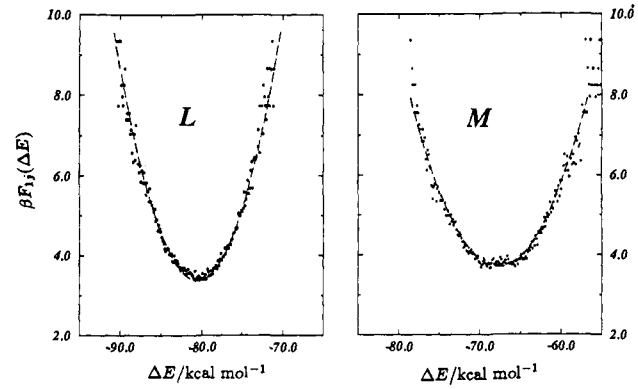

Figure 6. Energy gap free energy surfaces in units of k_BT for model II. The filled circles are the results from simulations and the dashed lines are a second-order polynomial fit. The left panel shows the free energy $F_{13}(\Delta E)$ and the right panel shows the free energy $F_{13'}(\Delta E)$.

electron transfer makes it possible to derive the diabatic free energy surfaces for electron transfer from our simulation. The probability distributions for these gaps are defined in eq 2.10. We compute the prescribed distributions from histograms based on our trajectories. The corresponding free energies are

$$F_{ij}(\Delta E) = -k_B T \ln P_{ij}(\Delta E) \tag{4.5}$$

During an equilibrium simulation only a small region of the available phase space is sampled. The range of this region grows with the length of the simulation. In our calculations which lasted typically ~60 ps, we found that the system accessed regions of the free energy surface separated at most by $7k_BT$. This was sufficient to have a good estimate of the shape and curvature of the diabatic surfaces. In order to explore regions of phase space of higher free energy, some type of non-Boltzmann sampling would have had to be performed.

As typical examples of our results, in Figures 5 and 6 we present the free energy functions for the SP* → SP$^+$BPL$^-$ and SP* → SP$^+$BPM$^-$ energy gaps for models I and II. For both models these are parabolic within the statistical error. In the fit that we carried out to determine the curvature, the additional inclusion of the cubic term improved the χ^2 of the fit by at most 1%.

This result is similar to the findings of previous simulations of medium response in polar liquids.[31] Parabolic fits to estimates of energy gap free energies of the RC are also found in ref 16. The harmonicity of the energy gap energetics is consistent with the electron-transfer model described in Section 2 where we assumed a linear coupling between the three-level system and the bath. The harmonic behavior of the polarization free energy surface was first suggested by Marcus in his early works on electron transfer.[14]

The curvatures of the free energy parabolas calculated with model I are larger than those of model II. Since the major difference between the two models is the inclusion in model II of crystallization waters, hydration seems to increase significantly the reorganization energy of RC. In view of this result, hydration appears to play an important role in electron transfer.

Since equilibrium response of the solvent well approximated by a linear model does not imply a real time linear response, it is important to investigate the relaxation of the medium after electron transfer. For this purpose we have performed nonequilibrium molecular dynamics simulations for model I where one electron from the special pair was transferred instantaneously to the accessory bacteriochlorophyll on the L side. The trajectories illustrated in Figure 2 would indicate that the assumed linear behavior might be most problematical with regard to the accessory bacteriochlorophylls. The transition we considered was from a neutral SP* state to a charge-separated SP$^+$BCL$^-$ state. As is consistent with eqs 4.1 and 4.2, the charge distribution of the latter state was obtained by adding charges 0.125e and –0.25e, respectively, to the nitrogens of the SP and BCL. The nonequilibrium runs started from a few equilibrated configurations of particles and velocities in the neutral SP* state. At time zero, the electronic state was switched from SP* to SP$^+$–BCL$^-$. The system was then allowed to evolve for a few hundred femtoseconds with the new charge distribution governing the molecular dynamics. During this period, the energy gap, ΔE_{12} as given by eqs 4.1–4.3, was monitored. If the system exhibits linear response, the averaged nonequilibrium energy gap relaxation, $\overline{\Delta E}_{12}(t)$ should obey the fluctuation dissipation theorem, namely

$$\frac{\overline{\Delta E}_{12}(t) - \langle \Delta E_{12} \rangle_2}{\overline{\Delta E}_{12}(0) - \langle \Delta E_{12} \rangle_2} = \frac{C_{12}(t)}{C_{12}(0)} \tag{4.6}$$

where the overbar indicates an average over many nonequilibrium trajectories, each prepared as described above. The ultimate equilibrated value of $\overline{\Delta E}_{12}(t)$, namely, $\langle \Delta E_{12} \rangle_2$, was computed from a separate 20-ps run with the state 2 potential surfaces. Note that the relaxation examined here takes place on the diabatic state 2, but the correlation function $C_{12}(t)$ is computed on state 1 (eq 4.4). Thus, eq 4.6 is a severe test of linear behavior. One might imagine comparing the nonequilibrium relaxation in state 2 with autocorrelation functions computed for that same state. Such a comparison, however, would not fully test the reduced model Hamiltonian discussed in Section 2. Not surprisingly, when put to the test, we can observe deviations from linear behavior.

In Figure 7a, we compare the calculated nonequilibrium relaxation with that predicted by linear response. In order to obtain an acceptable statistical error, the nonequilibrium results are averaged over 140 runs. Each simulation was run for 250 fs. We observe that many of the fast modes predicted by linear response are present in the nonequilibrium experiment. However, the nonequilibrium curve decays to the long time average in the final state more slowly than the equilibrium prediction. In Figure 7b, we show the result of a set of 60 more nonequilibrium simulations carried on for 600 fs each. The statistics, of course, are not as good as that in Figure 7a. Nevertheless, we see that, after 0.6 ps, the nonequilibrium runs are nearly converged to the equilibrium prediction. Our findings show that the dynamical response of the proteic environment has noticeable nonlinear behavior. After electron transfer a structural relaxation on a picosecond time scale occurs.

The nonlinear behavior we have exhibited is of a quantitative and not qualitative nature. Further, it is observed in the dynamics and not the free energy surfaces. We therefore adopt the harmonic model of Section 2 as a reasonable caricature. In Section 5 we first discuss how the parameters of the reduced model have been

(31) Kuharski, R. A.; Bader, J. S.; Chandler, D.; Sprik, M.; Klein, M. L.; Impey, R. W. *J. Chem. Phys.* **1988**, *89*, 3248.

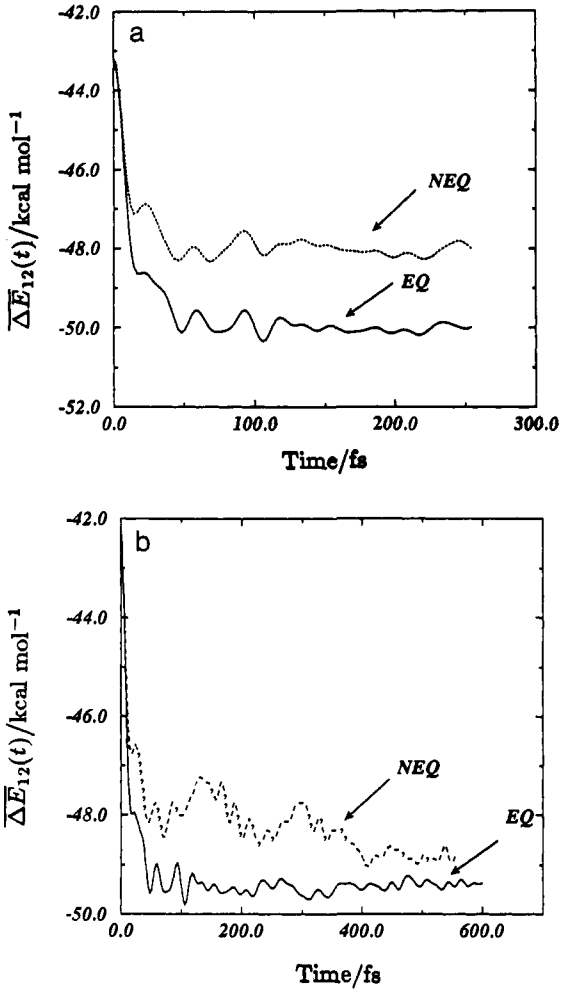

Figure 7. (a) Comparison between equilibrium correlation function and nonequilibrium relaxation. The continuous line is the linear response prediction based upon the time correlation of 56 ps of equilibrium simulation. The dashed line has been computed by averaging 140 nonequilibrium MD runs. The estimated statistical errors are within the thickness of the lines. (b) Comparison between equilibrium correlation function and nonequilibrium relaxation. The continuous line is the linear response prediction based upon the time correlation of 56 ps of equilibrium simulation. The dashed line has been computed by averaging 60 nonequilibrium MD runs. The statistical uncertainties are larger in this graph than in (a); see text for explanation.

obtained from simulation and then derive the diabatic free energies for electron transfer and the spectral densities of the relevant fields.

5. Scaled Reduced Model

Model II is the more realistic of the two atomistic models. It includes the crystallization water molecules and has a more detailed electrostatic description of the chromophores than model I. We limit our discussion now to the results obtained with model II.

As described in Section 2 and justified in Section 4, the electron transfer on the L (or M) branch can be roughly modeled in terms of three coupled harmonic diabatic surfaces. Using the simulation results for average energy gaps and fluctuations, we have evaluated the parameters in the model. In particular, we have used eqs 2.4 and 2.6 to identify $\Delta\epsilon_2$ and $\Delta\epsilon_3$. Further, we have used the curvatures of the simulation free energies $F_{12}(\Delta E)$ and $F_{13}(\Delta E)$ together with eqs 2.3, 2.5, 2.7, and 2.13 to identify $\alpha_\parallel$, $\alpha_\perp$, and b. The parameters obtained in this way are entered in Table I. We call these "basic parameters", as they arise straightforwardly from the molecular modeling we have performed. Notice that $\alpha_\parallel$ and $\alpha_\perp$ for the L branch are significantly smaller than those for the M branch. In other words, the mean square fluctuations

Table I. Basic Parameters

branch	$\Delta\epsilon_2$, kcal mol^{-1}	$\Delta\epsilon_3$, kcal mol^{-1}	$\alpha_\parallel$, kcal mol^{-1}	$\alpha_\perp$, kcal mol^{-1}	b
L	−33.68	−81.3	13.74	8.38	0.551
M	−36.45	−68.5	22.88	10.94	0.632

Table II. Electronic Energies

transition	$\Delta\epsilon_j^{(0)}$,[a] kcal mol^{-1}	$-v_j$,[b] kcal mol^{-1}
SP* → SP$^+$BCL$^-$	23.7	24.6
SP* → SP$^+$BPL$^-$	23.4	32.31
SP* → SP$^+$BCM$^-$	24.7	31.2
SP* → SP$^+$BPM$^-$	25.8	33.9

[a] The $1 \rightarrow j$ energy difference computed by Thompson and Zerner, ref 22. [b] v_j denotes the electrostatic contribution to the $1 \rightarrow j$ basic energy gap from the chromophores and four histidine amino acid side chains.

pertinent to electron transfer are much smaller in size on the L branch than on the M branch. This finding of greater rigidity of the L side is consistent with the fact that the L side contains more aromatic (nonpolar) residues than the M side. This contrast in rigidity, we will see, is related to the marked differences in activity between the L and M branches of the RC.

The diabatic curves defined by these parameters need to be adjusted to incorporate two important physical aspects of the system. We turn to these aspects now. First, we need to account for the ionization potentials and electron affinities associated with moving the electron from one chromophore to another. Second, we need to account for the role of electronic polarization in the proteic environment. Both are beyond the scope of a purely classical molecular dynamics simulation. We treat the first by incorporating information from Thompson and Zerner's computation of excitation energies for the chromophores.[22] We treat the role of electronic polarization by a scaling of our basic values for $\alpha_\parallel$, $\alpha_\perp$, and the corresponding solvation contributions to the average energy gaps. Justification for this scaling is discussed in the Appendix. Thompson and Zerner[22] performed INDO/S SCF-CI calculations for the electronic energies for the system composed of the four bacteriochlorophylls, the two bacteriopheophytins, and the four histidine amino acid side chains that coordinate with the Mg atom of the bacteriochlorophylls. In Table II, we report the excitation energies they calculated for the four charge transfer states relative to the singlet SP* electronic energy.

As defined in eqs 4.1–4.3, the basic energy gap includes electrostatic contributions from the chromophores, histidines and surrounding proteic environment. In order to use Thompson and Zerner's computed electronic energies, we have to first remove from the basic electrostatic energy gaps the contributions from the chromophores and histidines. We let v_j denote this electrostatic contribution to the $1 \rightarrow j$ energy gap. This contribution was computed explicitly by running another 10-ps simulation of the reaction center in the neutral state in the same conditions as before. We report this contribution in Table II. Because of the rigidity of the chromophores, the overall error bars on those energies are small, 0.5 kcal. We let $\Delta\epsilon_j^{(0)}$ denote the energy difference for the $1 \rightarrow j$ transition computed by Thompson and Zerner. Then

$$[\Delta\epsilon_j - v_j] + \Delta\epsilon_j^{(0)}$$

would be the classical average energy gap which incorporates Thompson and Zerner's numbers. The term in square brackets is a solvation contribution to the energy gap. In the Appendix we show that the influence of electronic polarization for this quantity may be incorporated by scaling the classical simulation result by the factor $1/\epsilon_\infty$. This scale factor rests on the approximation that the electronic polarizability is isotropic and uniform throughout the proteic environment.) Hence the physically relevant average energy gaps, $\Delta\bar{\epsilon}_j$, are obtained from the

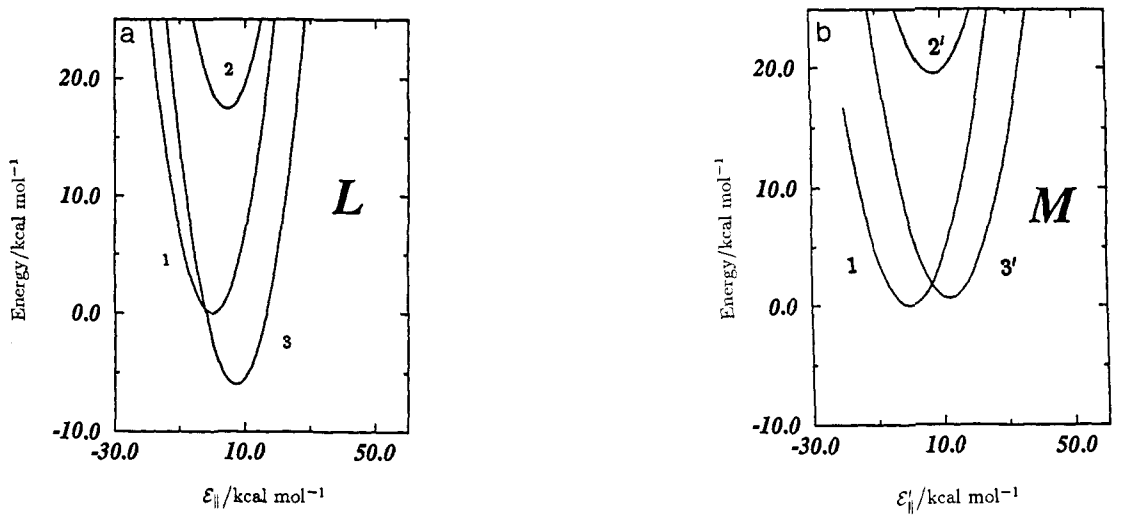

Figure 8. (a) Diabatic free energy surfaces of the three-level spin-boson model as calculated by the atomistic model II for the L branch. See text for explanation of the parameters used in the plot. Note that $\mathcal{E}_\perp = 0$ in this plot. (b) Diabatic free energy surfaces of the three-level spin-boson model as calculated by the atomistic model II for the M branch. See text for explanation of the parameters used in the plot. Note that $\mathcal{E}'_\perp = 0$ in this plot, and that $\mathcal{E}'_\parallel$ is a different variable than $\mathcal{E}_\parallel$ in (a).

Table III. Scaled Parameters Governing Diabatic Free Energy Surfaces

branch	$\Delta\bar{\epsilon}_2$, kcal mol^{-1}	$\Delta\bar{\epsilon}_3$, kcal mol^{-1}	$\bar{\alpha}_\parallel$, kcal mol^{-1}	$\bar{\alpha}_\perp$, kcal mol^{-1}	b
L	18.9	−2.4	7.23	4.41	0.551
M	21.9	7.63	12.0	5.76	0.632

classically simulated gaps, $\Delta\epsilon_j$, by the transformation

$$\Delta\epsilon_j \rightarrow \Delta\bar{\epsilon}_j = \Delta\epsilon_j^{(0)} + (\Delta\epsilon_j - v_j)/\epsilon_\infty \qquad (5.1)$$

These adjustments require a value for the "optical dielectric constant", ϵ_∞. We fit this number empirically so as to ensure that the computed thermodynamic driving force for SP* → SP$^+$BPL$^-$ agrees with experiment. In particular, the scaled model gives the driving force

$$\Delta G_{13} = -(\bar{\alpha}_\parallel/2) + \Delta\bar{\epsilon}_3 \qquad (5.2)$$

where $\bar{\alpha}_\parallel = \alpha_\parallel/\epsilon_\infty$ is the scaled nuclear polarization susceptibility. See eqs A.16 and A.17. The quantity $\bar{\alpha}_\parallel/2$ is the scaled reorganization energy[15] (λ_{13}) associated with states 1 and 3. The corresponding scaled expression for λ_{12} is given by $b^2\bar{\alpha}_\parallel/2 + \bar{\alpha}_\perp/2$.

With eqs 5.1, 5.2, and the data tabulated in Tables I and II, we can find a value of ϵ_∞ such that ΔG_{13} has the experimental value of −6 kcal/mol.[20,21] This fitting yields $\epsilon_\infty = 1.9$, which is in reasonable accord with the optical dielectric constants of most dense fluids (including room-temperature liquid water, for which $\epsilon_\infty \approx 1.8$). We regard this finding, that a physically reasonable value of ϵ_∞ brings our computed results into agreement with experiment, as an indication of success in our modeling of the RC. In Table III, we compile the parameters associated with the shifted and scaled reduced model. The parameter b does not change from Table I to Table III because we assume the electronic polarization fluctuations are distributed isotropically throughout the proteic system. Hence, $\alpha_\perp$ and $\alpha_\parallel$ are scaled by the same ϵ_∞, and eq 2.7 remains satisfied with no scaling of b.

Before discussing the nature of the resulting diabatic surfaces, we comment on the robustness of our results. The molecular dynamics calculations employ symmetric charge distributions on the chromophores. We have examined the possibilities of errors associated with these simplified distributions by carrying out additional trajectories with a dipolar distribution on the special pair. Indeed, experiment has determined that SP* is polar.[6,32] By moving a full electronic charge to the four nitrogens on the M side of SP (and a corresponding +e on the four nitrogens on the L side), we find that the basic energy gaps change by no more than 0.5 kcal. In other words, the changes are very small. They are a percent or less of the totals (see Table I).

Thus, it would appear that our conclusions will not be altered by the use of more sophisticated charge distributions of the central chromophores in the molecular dynamics calculations. On the other hand, at this time we are not able to assess the accuracy of Thompson and Zerner's energies. However, they enter into our analysis in a straightforward fashion, and adjustments are simple to make with the data provided herein if and when these numbers are revised.

Now consider the diabatic free energy surface implied by the scaled parameters listed in Table III. The $\mathcal{E}_\perp = 0$ slice of these functions is plotted in Figure 8. (Slices at other values of $\mathcal{E}_\perp$ provide a similar perspective.) We see that the intersection of states 1 and 3 (coinciding with the SP* → SP$^+$BPL$^-$ transfer) is slightly into the inverted region with almost no activation energy. In contrast, the corresponding intersection of states 1 and 3′ on the M branch occurs in the normal region with an activation energy of $\sim 4k_BT$ and an *endothermic* $\Delta G_{13'} \approx 1.6$ kcal/mol. This difference provides an explanation of the inactivity of the M branch within our model.

Next, notice the location of the accessory bacteriochlorophyll states, 2 and 2′. The minima of both surfaces lie approximately 15 kcal/mol above that of state 1. This finding agrees well with Thompson and Zerner's estimates of the solvation of states 2 and 2′. Using dielectric continuum theory, they predicted that states 2 and 2′ lie 14.4 kcal/mol above the initial SP* state.[22] The relative positioning that we predict for the charge-transfer state on the accessory bacteriochlorophyll implies that the primary electron transfer does not occur by a two-step mechanism. On the other hand, in Section 7, we argue that superexchange can support electron transfer on the L branch with a reasonable choice of the mean coupling matrix element, $\tilde{H} = (|H_{12}||H_{23}|)^{1/2}$.

An analysis of the electron transfer dynamics requires the power spectra of the energy gap fluctuations. We have computed these quantities for model II by Fourier transforming the time correlation functions, eq 2.14, scaling the zero time values of $C_\parallel(t)$ and $C_\perp(t)$ to coincide with $k_BT\bar{\alpha}_\parallel$ and $k_BT\bar{\alpha}_\perp$, respectively. That is,

$$C_\parallel(t) \rightarrow \bar{C}_\parallel(t) = k_BT\bar{\alpha}_\parallel C_\parallel(t)/C_\parallel(0) \approx \frac{1}{\epsilon_\infty} C_\parallel(t) \qquad (5.3)$$

and similarly for $C_\perp(t)$. We have also scaled $C_{cross}(t)$ by dividing by ϵ_∞. Whether or not $C_{cross}(t)$ should be scaled seems unimportant

(32) Lockhart, D. J.; Hammes, S. L.; Franzen, S.; Boxer, S. G. *J. Phys. Chem.* **1991**, *95*, 2217.

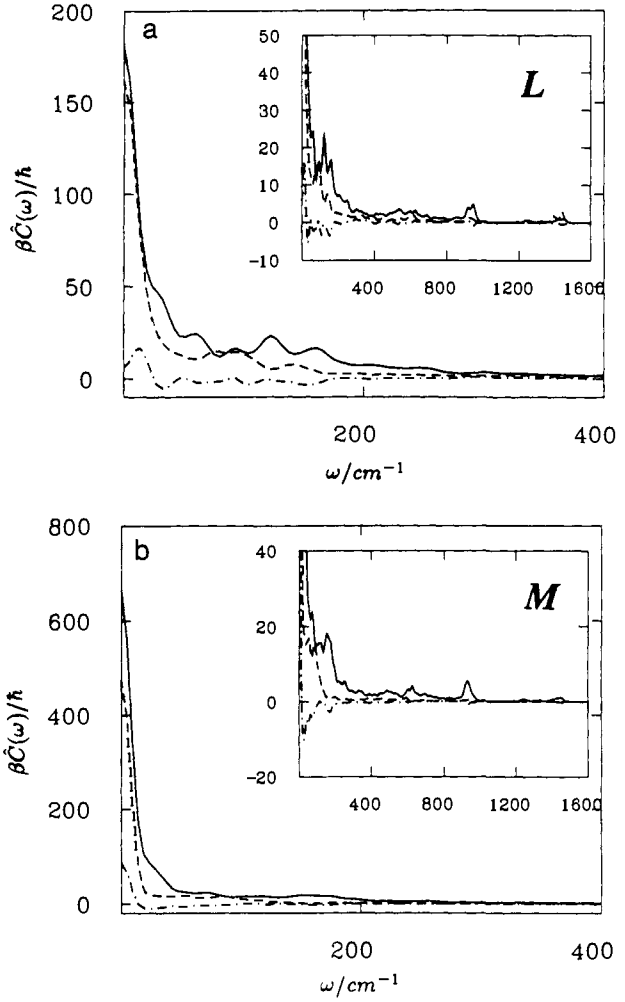

Figure 9. (a) Spectral densities $\hat{C}_{\parallel}(\omega)$ (solid line), $\hat{C}_{\perp}(\omega)$ (dashed line), and $\hat{C}_{cross}(\omega)$ (dot-dashed line) for the L branch. Inset shows these functions at large frequencies. (b) Spectral densities $\hat{C}_{\parallel}(\omega)$ (solid line), $\hat{C}_{\perp}(\omega)$ (dashed line), and $\hat{C}_{cross}(\omega)$ (dot-dashed line) for the M branch. Inset shows these functions at large frequencies.

since these cross correlations are relatively small. A Blackman window of 2.4 ps width was used in the Fourier transformation in order to remove artifacts in the spectrum that result from the finite length of time of the simulated correlation functions.[33] The three Fourier transforms for both the L and M branches are plotted in Figure 9. We see that the power spectra of $\mathcal{E}_{\parallel}$ and $\mathcal{E}_{\perp}$ have wide continuous ranges. It would seem difficult to capture this behavior with models involving only a few oscillators.

The spectra for the branch L and M have similar features, but differ in the details. In the region above 200 cm^{-1}, the differences are small. At low frequencies, however, the peaks differ in position and intensity. Additionally, the series of peaks between 98 and 160 cm^{-1} in the $SP^* \rightarrow SP^+BPL^-$ spectral density is replaced by one single peak around 190 cm^{-1} in the $SP^* \rightarrow SP^+BPM^-$ with an intensity twice as low. Also note that $\mathcal{E}_{\parallel}$ and $\mathcal{E}_{\perp}$ in our model are not only orthogonal at $t = 0$ (see condition 2.7), but as shown in Figure 9, a and b, they are approximately orthogonal in the entire frequency range and, therefore, the time domain.

6. Comparison with Previous Simulations

As we mentioned in the Introduction, in the past there have been two groups that have carried out simulation studies of photosynthetic reaction centers. Schulten's group has carried out a few nonequilibrium calculations of the reaction center of *Rps. viridis* at various temperatures.[17] Their approach is limited

(33) Allen, M. P.; Tildesley, D. J. *Computer Simulation of Liquids*; Clarendon Press: Oxford, 1987; pp 208–211. Harris, F. J. *Proc. IEEE* **1978**, *66*, 51–83.

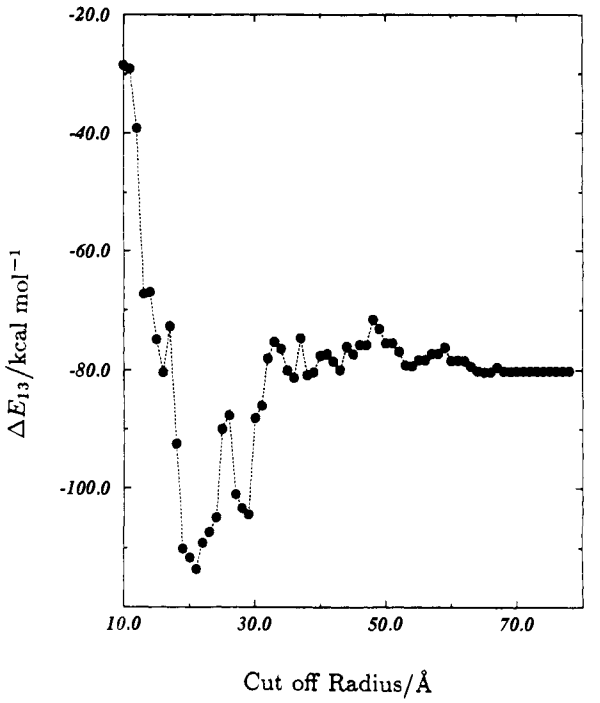

Figure 10. Energy gap ΔE_{13} for one nuclear configuration of model II as a function of the electrostatic potential energy cutoff radius.

to the study of the electron transfer reaction along the L branch, and they have performed no calculations concerning the inactivity of the M branch. Their nonequilibrium calculations consisted of only one run for each temperature in which one electron is transferred from SP to BPL. They inferred a linear behavior of the proteic media by comparison with an equilibrium 20-ps run. In this paper, we have shown that many nonequilibrium runs and long equilibrium simulations are needed to achieve sufficient statistics for the meaningful studies of linear behavior. We find statistically significant differences between equilibrium and nonequilibrium time correlation functions.

The electrostatics of Schulten's model is very similar to ours in model II. Nevertheless, the electrostatic contributions to the energy gaps reported by Schulten and co-workers differ from those that we compute by factors ranging from 3 to 8. Part of the disparity may be due to their truncations of Coulombic potentials. In ref 17b, a 10-Å cutoff is employed, while in ref 17d, a 40-Å cutoff is employed. Curiously, in both cases, the same value of the average $SP^* \rightarrow SP^+BPL^-$ energy gap is reported, –20 kcal/mol. To check the effect of radial cutoff on the computed energy gap, we have carried out a calculation of the energy gap between SP^* and SP^+BPL^- versus the electrostatic potential cutoff. This was done for the X-ray structure resolved at 2.3 Å. We included in the calculation the contributions from each residue and chromophore within the cutoff range of one of the redox sites. Our result in Figure 10 shows the expected oscillatory character typical of coulombic sums. We conclude that without accounting for screening by some other means, calculations at cutoffs lower than 60 Å are unreliable. We note that the four-protein complex considered in this work is approximately 120 Å in diameter. With this distance in mind, one can understand why the Coulombic sums converge at a cutoff near 60 Å.

Warshel, Parson, and their co-workers[16] have studied the fluctuations of the energy gap and in one case, for the electron transfer from BPL to the quinone,[16b] the spectral density and the diabatic free energy surfaces were calculated. Their diabatic free energies are defined in similar ways to ours, but their calculations of the contributions from various components are significantly different. In ref 16d, which is most related to the work in this paper, they estimated the free energies of the charge-separated states by a static calculation on the experimentally determined X-ray structure. Reorganization energies were also

estimated. The electrostatic contributions are computed by a truncated Coulomb sum and a dielectric continuum estimate for the effects of contributions beyond a short cutoff. Atomic polarizability is included through a classical computation of induction effects. Experimentally measured redox potentials of the chromophores in solution are used to account for the electronic energies of the unperturbed chromophores. The end result is a positioning of the diabatic energies that is very different from those we have found. Most significantly, they predict an unrelaxed SP^+BCL^- state at the same energy as SP*, and a SP^+BPL^- lower in energy by about 2 kcal/mol. This arrangement would support a two-step mechanism in the primary electron transfer, something which is incompatible with our results.

Our accounting of atomic polarizability is through the scaling which has quantum mechanical elements as discussed in the Appendix. Our accounting of dielectric screening is through the explicit addition of all Coulombic interactions in the proteic system. The surrounding polar environment is not accounted for, but this is far from the central chromophores. Finally, our use of experimentally calibrated INDO calculations to obtain the necessary redox potentials avoids theoretical uncertainties as to how one should best extract these numbers from solution-based experiments.

7. Conclusion

Our most important findings are summarized by Figure 8, which shows cuts through the diabatic free energy surfaces governing the primary electron transfer. The thermodynamic driving force for the forward reaction, ΔG_{13}, is fit with a reasonable value of $\epsilon_\infty \approx 1.9$. With no further adjustment, the simulation model predicts that the forward reaction is nearly activationless. It also predicts that the M branch is inactive as $\Delta G_{13'}$ is found to be positive. Both predictions about the respective activities agree with experiment. Further, according to the model, the mechanism to pass from state 1 (SP*) to state 3 (SP^+BPL^-) must evolve via superexchange with state 2 (SP^+–BCL^-). Let us now consider simple estimates of the primary electron transfer rate based upon superexchange and the diabatic surfaces we have computed.

The golden rule formula for the rate constant (treating the nuclear coordinates as classical variables) is

$$k_{1\to 3} = (2\pi/\hbar)K^2\langle\delta(\Delta E_{13})\rangle_1 \qquad (7.1)$$

where K is the effective coupling between states 1 and 3. With superexchange involving state 2, K is given by

$$K = (\bar{H}^2/\Delta E_{12})^* \qquad (7.2)$$

where $\bar{H}^2 = |H_{12}\|H_{23}|$, and the asterisk indicates that the quantities within the brackets are to be evaluated at the nuclear configurations where $\Delta E_{13} = 0$. (We neglect contributions to K that are higher order in $\bar{H}/\Delta E_{12}$ since, in light of our computed values for ΔE_{12}, reasonable estimates of $\bar{H}$ would demand that $\bar{H} \ll \Delta E_{12}$.) With parabolic free energy surfaces intersecting with essentially no activation energy, eqs 7.1 and 7.2 yield

$$k_{1\to 3} \approx \frac{2\sqrt{\pi}}{\hbar}\left(\frac{\bar{H}^2}{\Delta\bar{\epsilon}_2}\right)^2 \frac{1}{(k_B T\bar{\alpha}_\parallel)^{1/2}} \qquad (7.3)$$

Evaluation at room temperature based upon the entries in Table III gives $k_{1\to 3} \approx (\bar{H}/200\ \text{cm}^{-1})^4/25$ ps. Hence, an electronic coupling between nearest-neighbor chromophores of 250 cm^{-1} to 300 cm^{-1} is consistent with the experimentally observed[4,8] time scale for the primary transfer, 3 to 10 ps. Such values for electronic couplings seem physically reasonable.[34]

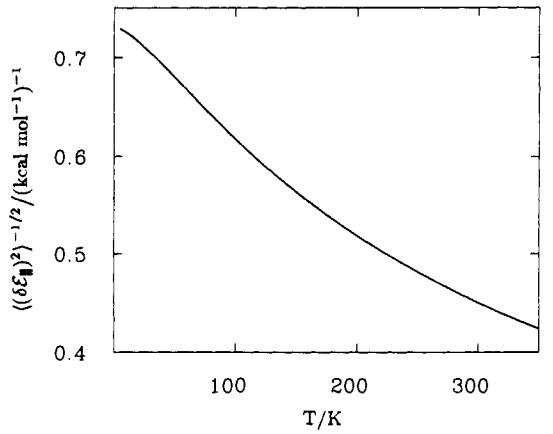

Figure 11. Temperature dependence of $\langle(\delta\mathcal{E}_\parallel)^2\rangle^{-1/2}$. Here, $\langle(\delta\mathcal{E}_\parallel)^2\rangle$ has been evaluated from the spectral density with the formula $\langle(\delta\mathcal{E}_\parallel)^2\rangle = \beta\hbar(4\pi)^{-1}\int_0^\infty d\omega\ \tilde{C}_\parallel(\omega)\omega\coth(\beta\hbar\omega/2)$.

There has been some discussion in the literature relating the singlet–triplet splittings of states 1 and 3 that would indicate the nearest-neighbor couplings are significantly smaller than 10^2 cm^{-1}.[35] By invoking only states 1, 2, and 3 with superexchange coupling, Marcus has related the measured splittings[36] to H_{12}, H_{23} and the relative positioning of the three surfaces. When we combine the measured splittings with our computed diabatic surfaces, Marcus' relationship yields $\bar{H} \approx 50$ cm^{-1}, nearly an order of magnitude smaller than we find based on our analysis of the electron transfer kinetics. We suspect, therefore, that the mechanism for the singlet–triplet splittings involves more states than simply 1, 2, and 3. In view of this uncertainty, however, it is worthwhile to compare predictions of our model with experimental observations that are independent of these nearest-neighbor couplings.

For example, the experimental observation that the forward transfer rate increases with lowering of temperature[30] is consistent with our results. We can already see this tendency in the classical result, eq 7.3. The increase in rate is due to the diminution of $\langle(\delta\mathcal{E}_\parallel)^2\rangle_1$ with decreasing T. In the classical limit, this rms fluctuation is given by $k_B T\bar{\alpha}_\parallel$. In reality, however, zero-point motion prohibits it from vanishing at $T\to 0$, and the temperature dependence of the rate is less dramatic than might be inferred from eq 7.3. We have carried out the quantal evaluation of $\langle(\delta\mathcal{E}_\parallel)^2\rangle_1$ with the aid of the spectral density given in Figure 9. Our result is graphed in Figure 11. It indicates a nearly 2-fold increase in rate in passing from room temperature to cryogenic temperatures. This behavior is in reasonable accord with experiment.[30] At this stage more detailed calculations for low-temperature experiments is not merited since the diabatic surfaces we have computed are probably not yet positioned to the extreme accuracy required to analyze cryogenic behavior.

As another example, we consider the rate of the back-reaction to the unexcited SP, i.e., SP^+–$BPL^-\to$SP. For the *Rhodobacter*

(34) We base our assertion of physical reasonableness on what we know to be true for the aqueous ferrous–ferric exchange (see: Logan, J.; Newton, M. D. *J. Chem. Phys.* **1983**, *78*, 4086. Marchi, M.; Chandler, D. *J. Chem. Phys.* **1991**, *95*, 889–894). For this relatively simple system, both wave function and path integral calculations give couplings of the order of 100 cm^{-1} for redox sites separated by about 6 Å. Given the nature of the interactions, we would expect similar couplings between two neighboring porphyrin rings. Nevertheless, nearest-neighbor electronic coupling matrix elements roughly an order of magnitude smaller than those we predict have been obtained with semiempirical quantum mechanical methods. A representative selection of such methods applied to the RC can be found in: Plato, M.; Mobius, K.; Michel-Beyerle, M. E.; Bixon, M.; Jortner, J. *J. Am. Chem. Soc.* **1988**, *110*, 7279–7285. Scherer, P. O. J.; Fischer, S. F. *Chem. Phys.* **1989**, *131*, 115–127. The discrepancy between these predictions and our findings remains unresolved. The discrepancy is not, however, necessarily incompatible with our acceptance of the energies reported in ref 22. The couplings or off-diagonal elements depend sensitively upon the tails of electron wave functions. A semiempirical calculation calibrated for diagonal elements can give accurate on-site energies yet inaccurate interstate couplings.

(35) Marcus, R. A. *Chem. Phys. Lett.* **1987**, *133*, 471–477. Bixon, M.; Jortner, J.; Michel-Beyerle, M. E. *Biochim. Biophys. Acta* **1991**, *1056*, 301–315.

(36) Moehl, K. W.; Lous, E. J.; Hoff, A. J. *Chem. Phys. Lett.* **1985**, *121*, 22–27. See also ref 37.

sphaeroides reaction center, experiment[37] has determined that its rate constant, k_b, is approximately 7000 times smaller than that of the forward $SP^* \rightarrow SP^+-BPL^-$ rate constant, $k_{1\rightarrow 3}$. We can compute a rate for the back-reaction from our computed spectral densities, and the measured vertical energy gap[38] between SP and SP*. The assumption that the nearest-neighbor electronic coupling between SP and BCL is approximately the same as that between SP* and BCL leads us to the effective superexchange back-reaction coupling of

$$K_b = (\bar{H}^2/\Delta E_{23})^* \tag{7.4}$$

Here, the superscript * indicates that ΔE_{23} is to be evaluated at the value of $\mathcal{E}_\parallel$ where $\Delta E_{03} = H_0 - H_3 = 0$. The quantity H_0 is the diabatic surface for the unexcited SP,

$$H_0 = H_1 - \Delta\epsilon_{01} \tag{7.5}$$

where $\Delta\epsilon_{01} \approx 30(\pm 3)$ kcal/mol is the above-mentioned measured vertical excitation energy. According to eqs 7.4, 7.2, and our computed diabatic surface parameters, Table III, the measured $\Delta\epsilon_{01}$ gives $K_b \approx 0.56K$. Further, the value of $\Delta\epsilon_{01}$ and our diabatic surface parameters place the intersection of the SP state with state 3 to be in the inverted region with a classical activation energy of approximately 28 kcal/mol. This large activation energy leads to the classical estimate, $k_b^{(cl)}/k_{1\rightarrow 3} \approx (0.56)^2 \exp(-45) \approx 10^{-20}$. The difference between this extreme underestimate and the experimental observation of $k_b \approx 10^{-4}k_{1\rightarrow 3}$ is largely due to nuclear tunneling. Nuclear tunneling provides the dominant pathway for the back-reaction because the 0 and 3 surfaces are spatially very close at their extreme inverted intersection. To compute the rate, one must therefore use the quantum version of the golden rule rate constant. With the stationary phase approximation,[39] it yields

$$k_b = (2\pi/\hbar)K_b^2|\nu^3(t^*)/2\pi\hbar\nu''(t^*)|^{1/2} \tag{7.6}$$

where $\nu(t^*)$ and $\nu''(t^*)$ are respectively the function and second derivative of

$$\nu(t) = \exp\left\{-(1/4\pi\hbar)\int_0^\infty d\omega\, \beta\hat{C}_\parallel(\omega)\left[\cosh(\beta\hbar\omega/2) - \cosh\left(\frac{\beta\hbar\omega}{2} - \omega t\right)\right]/\omega\sinh(\beta\hbar\omega/2)\right\}\exp(\Delta G_{03}t/\hbar) \tag{7.7}$$

evaluated at its extremum $t = t^*$ with $\Delta G_{03} = \Delta G_{13} + \Delta\epsilon_{01} \approx 24$ kcal/mol. From these formulas, we have evaluated k_b giving $k_b \approx 10^{-6}k_{1\rightarrow 3}$. The classical and quantal results differ by 14 powers of ten! The spectral density we have computed from our model, $\hat{C}_\parallel(\omega)$, accounts for 14 of the 16 orders of magnitude in $k_b^{(cl)}/k_b^{(expt)}$. Through sensitivity analysis, we have determined that no reasonable alteration of $\hat{C}_\parallel(\omega)$ will account for the additional two orders of magnitude. Nor will uncertainties in $\Delta\epsilon_{01}$, nor even a 5-kcal/mol variation in the position of H_2, account for this factor of 10^2. However, it is surely possible that anharmonic contributions to our diabatic free energy surfaces may alter the harmonic estimate of the high activation energy by 10%. This possible variation, 3 kcal/mol, would account for a factor of 10^2. In that case, better agreement with experiment would be fortuitous. This possibility of anharmonic contributions can be studied by future computer simulations which could examine the diabatic surfaces at high-energy configurations through the type of umbrella sampling technique exploited in ref 31. It could also be that the difference between our calculation and experiment is simply a manifestation of the differences between the *sphaeroides* system (for which the experiments have been done) and the *viridis* system (for which our present calculations are done). This possibility could also be examined with future molecular dynamics studies as well as with experiment.

Concerning time scales, bear in mind that 1 to 10 ps is not much longer than the relaxation times we have observed for nuclear motion. Thus, a simple rate constant description for the primary charge transfer may be inappropriate. Experimental observations of the SP* population decay may therefore involve a coherence between the nuclear motions and the electronic transitions. Jean et al.[40] have considered the role of such coherence in a related problem (though the spectral density they employ would not seem realistic for the RC). Exact quantum dynamical calculations based upon our computed spectral densities could resolve the importance of quantum coherence in the RC primary electron transfer. Given that the energy gap fluctuations decay primarily on a subpicosecond time scale (see Figures 3 and 4), it is unlikely that coherence associated with these particular motions are responsible for the observation of nonexponential decay in the SP* state on post-picosecond time scales. Rather, according to our model, motions affecting K must be responsible for the nonexponential relaxation.

Future work should address these dynamical issues. We hope that accurate calculations of the nearest-neighbor couplings, H_{12} and H_{23}, will become available. Modeling work on mutated versions of the RC would also be worthwhile. Of course, just as we have found necessary herein, this type of extension will require input from accurate quantum chemical calculations.

In general, we believe this paper demonstrates the power of molecular dynamics studies of biologically relevant systems. For well-defined molecular models, with sufficient care, the method can provide clear and robust predictions of the molecular mechanisms of biological function.

Acknowledgment. We have benefitted from conversations with Ron Levy, Richard Friesner, and Steven Boxer. One of us (M.M.) thanks Jeremy Smith and Giovanni Ciccotti for their kind hospitality and encouragement during the final stages of this work. In its early stages, this research was supported by the U.S. Department of Energy. The major part of this work was supported by the National Science Foundation through funding (Grant FD90-06235) and extensive access to the San Diego Super Computer Center. Some of our calculations and graphical visualization were performed with computers purchased in part with grants from the National Institutes of Health (Grants R01 GM37307 and 850RR05651A). The work done at Brookhaven National Laboratory (M.D.N.) was carried out under Contract DE-AC02-76CH00016 with the U.S. Department of Energy and supported by its Office of Basic Energy Sciences.

A. Appendix: Fast and Slow Polarization

In relating our classical simulation to experiment, we reduced the classical response functions and solvation contributions to the energy gaps by the ratio of the Pekar factor to the Born factor,

$$\left(\frac{1}{\epsilon_\infty} - \frac{1}{\epsilon}\right)\Big/\left(1 - \frac{1}{\epsilon}\right) \approx 1/\epsilon_\infty \tag{A.1}$$

The vertical energy gap may be expressed as the sum of a reorganization energy, λ, and a driving force, ΔG. For λ, the necessity for such a correction involving the optical dielectric constant, ϵ_∞, would seem apparent from Marcus's early work on electron transfer.[14] However, it can be shown that the same

(37) Norris, J. R.; Bowman, M. K.; Budil, D. E.; Tang, J.; Wraight, C. A.; Closs, G. L. *Proc. Natl. Acad. Sci. U.S.A.* **1982**, *79*, 5532–5536.

(38) Kirmaier, C.; Holten, D. *Photosynth. Res.* **1987**, *13*, 225–260.

(39) Van Duyne, R. P.; Fischer, S. F. *Chem. Phys.* **1974**, *5*, 183. See also Appendix 4 of ref 19. For the spectral density and driving force of the back-reaction we have computed the golden rule rate constant numerically by distorting the contour of integration to pass through the stationary phase point t^*. This exact numerical calculation agrees with the stationary phase estimate, eq 7.6, to better than 10%. The stationary phase estimate should not be confused with the semiclassical approximation employed in, for example, ref 16b.

(40) Jean, J. M.; Friesner, R. A.; Fleming, G. R. *J. Chem. Phys.* **1992**, *96*, 5827.

correction applies to the ΔG term. We outline here an argument that establishes these corrections and clarifies the underlying physics.[41]

The principal issue involves the different roles of slow and fast polarization modes. The former is the result of the nuclear reorganization in response to and affecting the redistribution of the transferring charge. The latter refers to the very high-frequency electronic polarization of the environment. Both types of polarizations contribute to the zero-frequency response and dielectric constant, ϵ. In contrast, the slow polarization modes are most pertinent to electron transfer. The distinction requires a quantum mechanical analysis that is beyond the scope of a classical computer simulation which utilizes potentials of interaction that are designed to duplicate the zero-frequency dielectric behavior. Nevertheless, the classical simulation provides information from which the quantum mechanical result can be reasonably estimated.

To see why, consider the following two-state system coupled to a bath (the generalization to three states is straightforward):

$$\mathrm{H} = -K[|1\rangle\langle 2| + |2\rangle\langle 1|] + |1\rangle[H_B - \mathcal{E}^{(s)} - \mathcal{E}^{(f)}]\langle 1| + |2\rangle[H_B + a^{(s)}\mathcal{E}^{(s)} + a^{(f)}\mathcal{E}^{(f)} + \Delta\epsilon^{(0)}]\langle 2| \quad (A.2)$$

where H_B is a bath Hamiltonian controlling the slow and fast Gaussian polarizations, $\mathcal{E}^{(s)}$ and $\mathcal{E}^{(f)}$, respectively. The constant $\Delta\epsilon^{(0)}$ allows for asymmetry resulting from differences in electronic energies at the different sites, while the parameters $a^{(s)}$ and $a^{(f)}$, which would be 1 in a symmetric system, allow for asymmetry in the system-bath coupling. The inclusion of a possible asymmetry in the system-bath coupling is irrelevant to the energy differences in the classical case as can be demonstrated by a simple transformation of variables. In the quantal case, however, the asymmetry could be important, and the fast polarization could have a different asymmetry than the slow polarization. All possible asymmetries are accounted for with $a^{(f)}$, $a^{(s)}$, and $\Delta\epsilon^{(0)}$. Hence, the model can be constructed such that

$$\langle\mathcal{E}^{(f)}\rangle_B = \langle\mathcal{E}^{(s)}\rangle_B = 0 \quad (A.3)$$

where $\langle\ldots\rangle_B$ indicates the equilibrium average over the bath uncoupled to the two-state system.

According to the Hamiltonian A.2, the action in Euclidean time is[19]

$$S = S_{TLS} + S_B[\mathcal{E}^{(f)}(t), \mathcal{E}^{(s)}(t)] + \hbar^{-1}\int_0^{\beta\hbar} dt\,\{h_1(t)[\mathcal{E}^{(f)}(t) + \mathcal{E}^{(s)}(t)] - h_2(t)[a^{(f)}\mathcal{E}^{(f)}(t) + a^{(s)}\mathcal{E}^{(s)}(t) + \Delta\epsilon^{(0)}]\} \quad (A.4)$$

where S_{TLS} is the action for an unperturbed symmetric two-level system with interstate coupling K, S_B denotes the action of the bath, and

$$h_1(t) = 1 - h_2(t) \quad (A.5)$$

is 1 if the system is in state 1 at time t and zero otherwise. The fast electronic polarization can be removed through standard Gaussian functional integration yielding the reduced action

$$\bar{S} = S_{TLS} + \bar{S}_B[\mathcal{E}^{(s)}(t)] + \hbar^{-1}\int_0^{\beta\hbar} dt\,\{h_1(t)\mathcal{E}^{(s)}(t) - h_2(t)[a^{(s)}\mathcal{E}^{(s)}(t) + \Delta\epsilon^{(0)}]\} + \frac{1}{2}\hbar^{-2}\int_0^{\beta\hbar} dt\int_0^{\beta\hbar} dt'\,[h_1(t) - a^{(f)}h_2(t)][h_1(t') - a^{(f)}h_2(t')]\langle\mathcal{E}^{(f)}(t)\mathcal{E}^{(f)}(t')\rangle_B \quad (A.6)$$

where $\bar{S}_B$ is a quadratic (and perhaps renormalized) functional of $\mathcal{E}^{(s)}(t)$.

(41) The argument is a slight generalization of that which we employed in: Gehlen, J. N.; Chandler, D.; Kim, H. J.; Hynes, J. T. *J. Phys. Chem.* **1992**, *96*, 1748. See also: Gehlen, J. N.; Chandler, D. *J. Chem. Phys.* **1992**, *97*, 4958.

No approximation has been made in arriving at eq A.6 from A.4. Having removed a degree of freedom, $\mathcal{E}^{(f)}$, the resulting action is nonlocal in time. Thus, in general, a Hamiltonian description would no longer be possible. But for the special case in which $\mathcal{E}^{(f)}$ is a fast variable (fast on the time scales set by $\hbar/K$ and $\beta\hbar$), further reduction is possible. In particular, the correlation function in the last term of eq A.6 is effectively a delta function,

$$\langle\mathcal{E}^{(f)}(t)\mathcal{E}^{(f)}(t')\rangle_B = \hbar\alpha^{(f)}\delta(t-t') \quad (A.7)$$

where

$$\alpha^{(f)} = \beta\langle(\mathcal{E}^{(f)})^2\rangle_B \quad (A.8)$$

With eq A.7, the reduced action is

$$\bar{S} = S_{TLS} + \bar{S}_B[\mathcal{E}^{(s)}(t)] + \hbar^{-1}\int_0^{\beta\hbar} dt\,\left\{h_1(t)\left[\mathcal{E}^{(s)}(t) + \frac{1}{2}\alpha^{(f)}\right] - h_2(t)\left\{\left[a^{(s)}\mathcal{E}^{(s)}(t) + \Delta\epsilon^{(0)} - \frac{1}{2}(a^{(f)})^2\alpha^{(f)}\right]\right\}\right. \quad (A.9)$$

from which diabatic Hamiltonians are readily constructed. They are

$$H_1 = \bar{H}_B - \mathcal{E}^{(s)} - \frac{1}{2}\alpha^{(f)}$$
$$H_2 = \bar{H}_B + a^{(s)}\mathcal{E}^{(s)} + \Delta\epsilon^{(0)} - \frac{1}{2}(a^{(f)})^2\alpha^{(f)} \quad (A.10)$$

where $\bar{H}_B$ is the (electronically averaged) bath Hamiltonian for the slow (nuclear) degrees of freedom.

Notice that one effect of averaging out the fast electronic polarization is to lower the energy of state 1 by $\alpha^{(f)}/2$, and to lower the energy of state 2 by $(a^{(f)})^2\alpha^{(f)}/2$. The net solvation energy, when the system is confined to state 1, is

$$\Delta\mu_1 = -k_BT\ln(\langle\exp[-\beta(H_1 - \bar{H}_B)]\rangle_B) = -\frac{1}{2}\alpha \quad (A.11)$$

where

$$\alpha = \alpha^{(s)} + \alpha^{(f)} \quad (A.12)$$

with

$$\alpha^{(s)} = \beta\langle(\delta\mathcal{E}^{(s)})^2\rangle_B \quad (A.13)$$

The second equality of eq A.11 is the result of performing the Gaussian average over the bath. From that result, we see that the fast and slow polarizations contribute in a similar fashion to the equilibrium solvation. In contrast, the two polarizations contribute in markedly different ways to the behavior of the energy gap, $\Delta E_{12} = H_2 - H_1$. For example, its average with the system confined to state 1 is

$$\langle\Delta E_{12}\rangle_1 = \Delta\epsilon^{(0)} - \frac{1}{2}[(a^{(f)})^2 - 1]\alpha^{(f)} + (a^{(s)} + 1)\langle\mathcal{E}^{(s)}\rangle_1 = \Delta\epsilon^{(0)} - \frac{1}{2}[(a^{(f)})^2 - 1]\alpha^{(f)} + (a^{(s)} + 1)\alpha^{(s)} \quad (A.14)$$

where the second equality follows from the Gaussian average of $\mathcal{E}^{(s)}$ with Hamiltonian H_1.

In a classical model of the bath, there are no high-frequency polarization fluctuations. Further, if the low-frequency components are tuned to give the correct solvation energetics, then $\alpha^{(f)} = 0$ and $\alpha^{(s)} = \alpha$. Such a classical model gives

$$\langle\Delta E_{12}\rangle_1^{(cl)} = \Delta\epsilon^{(0)} + (a^{(s)} + 1)\alpha \quad (A.15)$$

Notice the differences between this result and eq A.14. In an asymmetric system, the fast electronic polarization may solvate state 1 to a different extent than it solvates state 2. The resulting contribution to the average energy gap, $-[(a^{(f)})^2 - 1]\alpha^{(f)}/2$, is missed by the classical model. Further, the fluctuations in the energy gap scale with $\alpha^{(s)}$. For the classical model, these fluctuations scale with α. This difference in scaling results in the differences between the last terms of eqs A.14 and A.15.

An analogous comparison can be made concerning the thermodynamic driving force, ΔG_{12}. By computing the difference

between H_1 and H_2 at their respective minima, we find

$$\Delta G_{12} = \langle \Delta E_{12} \rangle_1 - (a^{(s)} + 1)^2 \alpha^{(s)}/2 \qquad (A.16)$$

This method for computing ΔG_{12} is correct because in the model the force constants governing fluctuations are the same in states 1 and 2. The reader may verify that the generally correct $\Delta G_{12} = \Delta\mu_2 - \Delta\mu_1$ gives the same result as (A.16) for this quantal model. In contrast to (A.16), the classical model gives

$$\Delta G_{12}^{(cl)} = \langle \Delta E_{12} \rangle_1^{(cl)} - (a^{(s)} + 1)^2 \alpha/2 \qquad (A.17)$$

The solvent reorganization energy, λ_{12}, described in traditional treatments of electron transfer,[15] can be defined in the present model according to

$$\langle \Delta E_{12} \rangle_1 = \lambda_{12} + \Delta G_{12} \qquad (A.18)$$

As a result, (A.16) gives

$$\lambda_{12} = (a^{(s)} + 1)^2 \alpha^{(s)}/2 \qquad (A.19)$$

while the classical model gives

$$\lambda_{12}^{(cl)} = (a^{(s)} + 1)^2 \alpha/2 \qquad (A.20)$$

The comparison of (A.19) and (A.20) is in agreement with Marcus' predicted scaling for these quantities.

Consider the consequences of this analysis to the protein molecular dynamics simulations reported in this paper. The molecular force field model was built from parameters designed to give a reasonable description of solvation. Hence, the average energy gaps one computes with the molecular dynamics coincide with (A.15) and the thermodynamic driving forces coincide with (A.17). Since, to a reasonable extent, the atomic structure of the protein complex is uniformly dense, the asymmetry associated with electron polarization is probably negligible, i.e., $a^{(f)} \approx 1$. As a result, the primary error of the classical model is in the energy gap fluctuations, which we see are too large by an amount $\alpha/\alpha^{(s)}$. This ratio is the reciprocal of the ratio of the Pekar factor to the Born factor, eq A.1.

In summary, the results of a classical simulation should be adjusted by (1) reducing the solvation contribution to the energy gap by the factor $\alpha^{(s)}/\alpha \approx 1/\epsilon_\infty$, and (2) reducing the mean-square fluctuations by $\alpha^{(s)}/\alpha \approx 1/\epsilon_\infty$, and increasing the free energy curvatures by $\alpha/\alpha^{(s)} \approx \epsilon_\infty$.

Provided the electronic polarization fluctuations occur isotropically throughout a proteic system, the same correction factors should be applied to all pairs of redox states. Note also that the same scale factor applies individually to ΔG_{12} and λ_{12} as well as to the total solvation portion of the energy gap.